Study of detectability of breast cancer with the ClearPEM scanner using gelatin phantoms

Ana Sofia Henriques de Vasconcelos Rodrigues
Under supervision of Dr. João Varela
Dep. Physics, LIP & IST, Lisbon, Portugal

***Abstract*—Breast cancer is one of the most common cancers among women and in 90% of these cases is curable if detected in time. In that respect, the Portuguese consortium PET-Mammography developed a scanner dedicated to breast imaging that allows the detection of reduced lesions, the ClearPEM.**
The aim of this work is to study the detectability of breast cancer with the ClearPEM scanner using gelatin phantoms developed for this study. The methodology included the quantification of the homogeneity (BV) and statistical noise (COV). Lesion detectability was evaluated using parameters such as lesion to background noise (LTBN) and lesion contrast recovery coefficient (CRC). A detailed analysis of the measurement of the lesions size was also performed.
Results indicate BV and COV of the order of 5-9% and 20-24%, respectively. ClearPEM images have been found globally homogeneous showing no artifacts. Small lesion to background ratio (LTB) and lesions of reduced dimensions howed less good contrast, but in most cases we report CRC values between 70% and 100%.
The detection of lesions is feasible down to 2 mm in diameter, so the overall assessment of the detector opens a promising perspective for the use of ClearPEM technology in clinical practice.

***Index Terms*—Breast Imaging, Positron Emission Mammography (PEM), ClearPEM, Detectability.**

I. Introduction

BREAST cancer has a high incidence rate and is 90% curable if detected in an early stage [1]. This type of cancer is the second leading cause of death in women, with a mortality of 1 in 35 cases [2], but this value has been decreasing as a result of improved early diagnosis and effective treatments.

Thus, the detection of breast cancer has become a priority in health policy on a increasing number of countries [3], and developments to deal with this problem are focused on clinical diagnosis at an early stage of the disease. Several imaging modalities are currently used in the detection of breast cancer; these include conventional x-ray mammography, ultra–sound (US), magnetic resonance imaging (MRI) and positron emission tomography (PET).

There is still a need for a diagnosis technology with higher specificity and sensitivity for early-stage tumors. In the next decade, the primary tool for screening breast cancer will have to involve high resolution and high contrast [4]. PET arises as a viable solution to this need. Nevertheless, although this technique has a sensitivity value greater than 90% in cases of large tumors, this value decreases to 25 % in small lesions [5]. The sensitivity in detecting lesions with a diameter smaller than 1 cm is around 57% [6] and, moreover, this value decrease in the detection of ductal carcinoma *in situ*, indicating a high number of false negatives. Due to these facts, PET is not clinically used in the evaluation of breast cancer unless the tumor size clearly suggests a high probability of distant metastatic disease [6]. In these cases, whole-body studies are conducted to assess the extent of the tumor. The development of dedicated imaging systems is crucial to improve these statistics.

The PET–Mammography consortium has developed a dual-head PET scanner dedicated to breast cancer imaging. The scanner called ClearPEM, uses APD-based detector modules in a double-readout scheme for depth of interaction (DOI) measurement in LYSO:Ce crystals. The DOI coordinate is determined from the asymmetry of the light collected on the two APD pixels reading out the same crystal [7].

The system was designed to image the breast region with higher spatial resolution and detection sensitivity than whole-body scanners. An example of the impact of the improvements in breast imaging by PEM systems, compared to whole-body PET scanners is shown in figures 1(a) and 1(b).

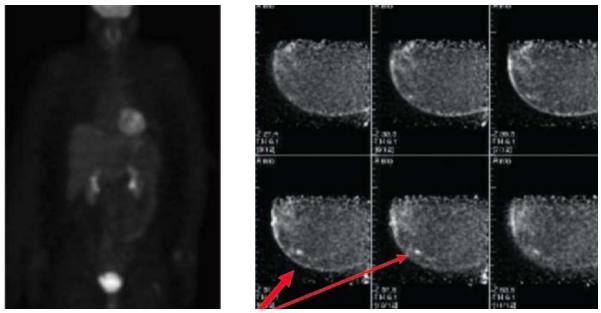

(a) **(b)**

Fig. 1. Whole-body PET (a) and PEM (b) scans. No evidence of cancer can be seen in the the whole-body PET scan image. The PEM scan revealed some abnormal ^{18}F-FDG uptake (red arrows) that marked the location of a ductal carcinoma [8]

Currently, the PEM technology has undergone clinical trials that demonstrate the potential of this technique in detecting breast cancer and its treatment planning [9]. The aim of this work is to determine the ClearPEM performance in pre–clinical tests using a novel and customized breast phantom. Simulated lesions of several sizes and different ratios of activity concentration between lesion and background ratio (LTB)

were evaluated using dedicated gelatin phantoms developed for this application. The methodology involved the quantification of image quality parameters such as homogeneity (BV), statistical noise (COV), ratio lesion to background noise (LTBN), contrast (CRC) and lesion reconstructed size.

II. Materials and Methods

Data from several gelatin phantoms were acquired and reconstructed for the analysis of image quality parameters. The phantoms are made with two basic materials that have similar properties to human tissues: gelatin and agar–agar. The phantoms consist of a cylindrical volume of 600 ml with diameter of 10 cm (featuring the background activity), where spherical lesions of different sizes (ranging from 1.5 mm up to 15 mm) were inserted.

A. Development of gelatin phantoms

First, 6 g of gelatin and 3 g of agar–agar are mixed in 600 ml preheated water. The entire mixture is then heated in a microwave until the liquid nearly boils ($\sim$ 5 minutes). After the addition of ^{18}F-FDG the mixture is placed in the freezer and allowed to harden. To make spherical lesions that simulate "tumors spherical volumes" we use molds created for this purpose. The same process is used with quantities of 3 and 0.6 g of gelatin and agar–agar, respectively, to 100 ml of water. The freezing time of "tumors spherical volumes" is 30 minutes and then they are removed from the molds and inserted into the semi-solid background phantom. Finally, the whole phantom is cooled in the freezer. The preparation of a gelatin phantom require approximately 1 hour.

The average uptake in the breast normal tissue is detailed in table I. In our study we have analyzed density category of "Fat with some fibroglandular tissue" and‘ "Extremely dense", with LTBs of 10:1, 5:1 and 2:1.

Breast tissue	**[^{18}F-FDG] (kBq/ml)**
Predominantly fat	1.59
Fat with some fibroglandular tissue	2.04
Heterogeneously dense	3.81
Extremely dense	4.81

TABLE I
^{18}F-FDG CONCENTRATIONS ACCORDING TO THE BREAST TISSUE RADIOGRAPHIC DENSITY CATEGORY [10]

Furthermore, we created other kind of phantoms for specific studies. To assess homogeneity, two phantoms without lesions were produced (phantom "water + FDG" and "gelatin + FDG"). The phantom "grid" (where lesions of 5, 4, 3, 2, and 1.5 mm are in matrix form without background), the phantom "cold" (which consists in a breast phantom with active lesions and a non active background) and the phantom "grid + background" (where the phantom "grid" was placed on a active background) were used to study the size of the lesions.

B. Gelatin phantoms imaging

Each phantom, centrally positioned between the two detector heads, was imaged using ClearPEM. The distance between the detector heads is 130 mm. Data was acquired in four orientations of the detector heads (90 °, 180 °, 135 ° and 225 ° rotation angles), each one during 15 minutes. The ClearPEM list-mode data format, allows the study of lower acquisition times by selecting offline the data acquired in smaller time intervals.

The acquired data was then reconstructed using the 3D iterative reconstruction algorithm OSMAPOL implemented in the STIR software [11]. No account for attenuation or random coincidence corrections was made. Every phantom was reconstructed with voxel size of $1 \times 1 \times 1.35\, mm^3$ and $2 \times 2 \times 1.35\, mm^3$, with and without simple Gaussian filter.

C. Statistical analysis

Homogeneity

The background variability (BV) was computed as proposed in NEMA NU-2 instructions (NEMA 2001) as:

$$BV = \frac{\sqrt{\frac{1}{R-1}\sum_{i=1}^{R}(\mu_i - \overline{\mu_i})^2}}{\overline{\mu_i}} \quad (1)$$

where μ_i is the average counts of each ROI, $\overline{\mu_i} = \frac{1}{R}\sum_{i=1}^{R}\mu_i$ is the average of ROI means over different ROIs, and R is the number of ROIs.

The method was to draw five regions of interest (ROI) in transaxial slices, for 30 slices, as shown in figure 2. The ROIs are circular and comprise the peripheral and central zone of the phantom. ROIs of various sizes were studied, namely 5, 10, 15, 20 and 25 mm of diameter.

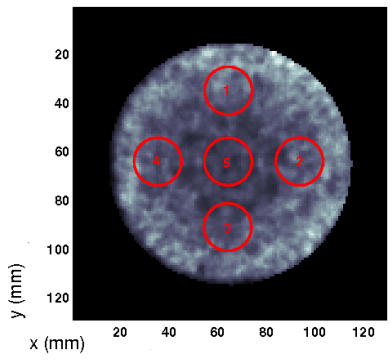

Fig. 2. Different space–positioned ROIs used to calculate percentage background variability in a central transaxial slice of phantom "water + FDG"

Noise

The image noise due to the voxel to voxel statistical variability in the image is defined as the coefficient of variation (COV) of the pixel values within a ROI as in:

$$COV = \frac{\sigma_{Bk}}{\mu_{Bk}} \quad (2)$$

where σ_{Bk} and μ_{Bk} represent the pixel standard deviation and average in a given background ROI. The procedure was the same as explain in the homogeneity.

Lesion To Background Noise

The LTBN was computed as follows:

$$LTBN = \frac{\mu_L - \mu_{Bk}}{\sigma_{Bk}} \tag{3}$$

In this definition μ_L denotes average counts in the lesion, μ_{Bk} is the average counts in background and σ_{Bk} represents the standard deviation of background.
For this purpose, circular ROIs were drawn over lesions and background. Surrounding each lesion ROI there are five background ROI of 20 mm of diameter. It is important to note that the diameter of the ROI used to define the lesion was taken as the FWHM of the Gaussian fit to the lesion profile.

Contrast

We have identified the real contrast (C_{real}) and reconstruction contrast (C_{rect}) which allows to compute a performance measurement, the Contrast Recovery Coefficient (CRC). By definition these parameters are given by:

$$C_{real} = \frac{L - Bk}{L + Bk} \tag{4}$$

$$C_{rect} = \frac{\mu L - \mu Bk}{\mu L + \mu Bk} \tag{5}$$

$$CRC = \frac{C_{rect}}{C_{real}} \tag{6}$$

The concentration of activity lesion is represented by L while Bk indicates concentration of activity background. On the other hand, the average counts of lesion and background are represented by μL and μBk, respectively. The method to determine these parameters was the same used to calculate the LTBN values.

Lesions size

In this work the size of the lesion was parameterized by the FWHM. As illustrated in figure 3, the estimation of the size of the reconstructed lesions is given by the FWHM of the Gaussian curves fitted to lesion profiles.

III. Results and Discussion

Homogeneity

We have studied the phantoms "water + FDG" and "gelatin + FDG" across all its FOV. Figure 4 shows the average number of counts per ROI (up to a normalization factor) as a function of the slice along the z-coordinate (phantom longitudinal axis). The data suggests that the height of the phantoms is not the same. It is visible that the phantom "gelatin + FDG" is smaller (covering slices 20–50) while phantom "water + FDG" cover slices 20–70. This decrease in volume was due to the boiling which was made when preparing the gelatin phantoms. On the other hand, the data obtained suggests the consistency of average value for all ROIs studied in the two phantoms. Only the values of ROI5 (central) are slightly lower which is caused by the lack of attenuation corrections.

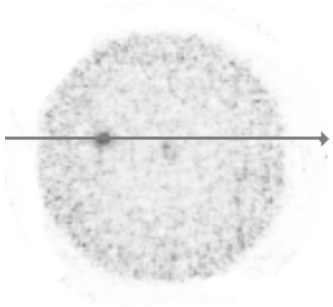

(a)

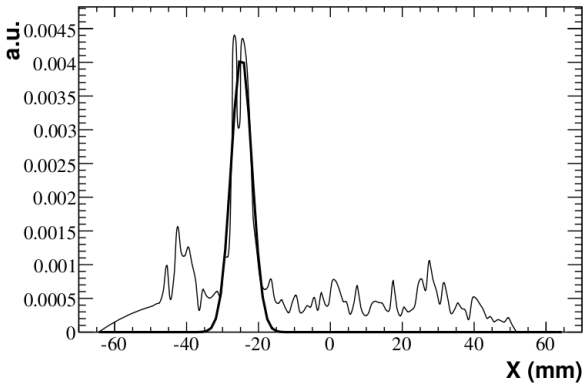

(b)

Fig. 3. Profile and its Gaussian curve of a 5 mm lesion into a phantom with LTB = 10:1 and reconstructed voxel size of $1 \times 1 \times 1.35\, mm^3$

A quantitative analysis of BV(%) was performed for the dimension of ROIs (5, 10, 15, 20 and 25 mm), its location and also for different acquisition times (5, 10 and 15 min). As detailed in figure 5 the BV(%) values decrease with rising ROIs sizes and the curves are similar for the two phantoms studied.

Table II validated that the BV(%) values are not significantly different for all ROI locations (with 20 mm of diameter) between two phantoms.

Ø 20 mm	**BV%**	
	"water + FDG"	**"gelatin + FDG"**
ROI1	6.0 ± 0.8	4.7 ± 0.6
ROI2	4.3 ± 0.6	3.2 ± 0.4
ROI3	3.8 ± 0.5	4.0 ± 0.5
ROI4	5.1 ± 0.7	6.2 ± 0.8
ROI5	7.1 ± 0.9	8.6 ± 1.1

TABLE II
BV(%) VALUES FOR EACH ROI LOCATION WITH 20 mm SIZE FOR PHANTOM "WATER + FDG" AND "GELATIN + FDG" RECONSTRUCTED WITH VOXEL SIZE OF $1 \times 1 \times 1.35\, mm^3$ AND ACQUISITION TIME OF 15 MIN

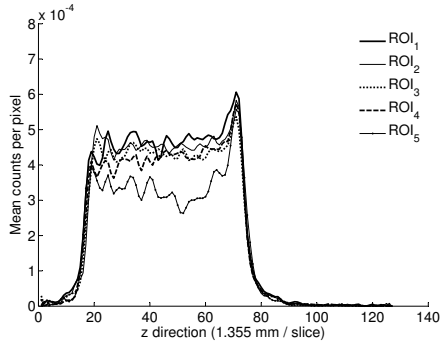

(a)

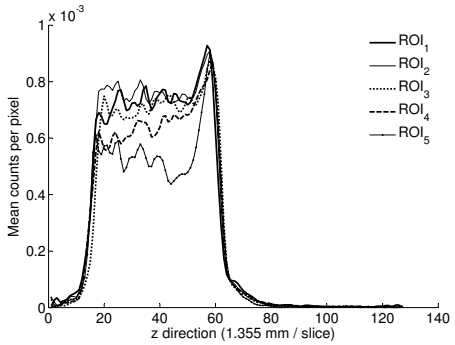

(b)

Fig. 4. Average counts per pixel (up to a normalization factor) across all FOV in direction Z, for all ROIs studied with 20 mm of diameter of phantom "water + FDG" (a) and "gelatin + FDG" (b) reconstructed with voxel size of $1 \times 1 \times 1.35\, mm^3$ and acquisition time of 15 min

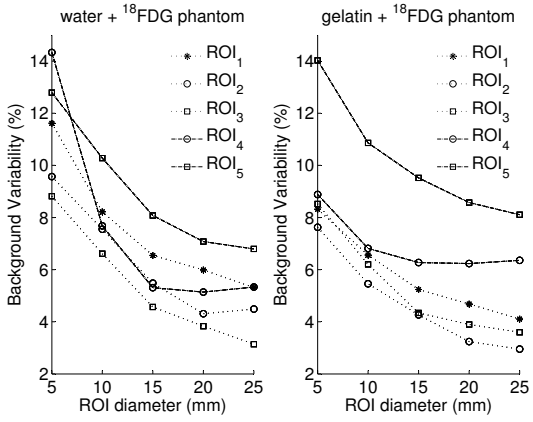

Fig. 5. BV (%) plotted versus ROI size for phantom "water + FDG" (left) and "gelatin + FDG" (right) reconstructed with voxel size of $1 \times 1 \times 1.35\, mm^3$ and acquisition time of 15 min

It can be seen from figure 6 that the BV(%) values drop with the decrease of acquisition time. However, this drop is not substantial, as the values are in the range 4%–9% for all acquisition times studie.

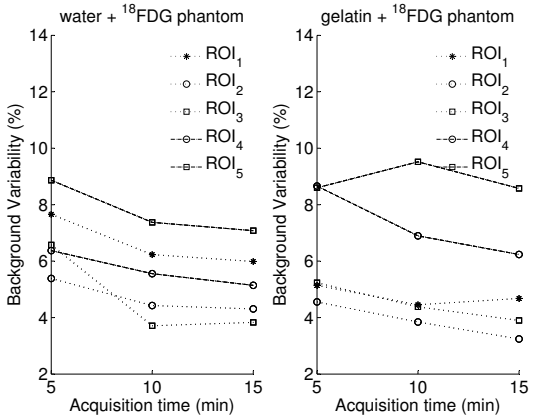

Fig. 6. BV (%) plotted versus acquisition time per detector orientation for phantom "water + FDG" (left) and "gelatin + FDG" (right) reconstructed with voxel size of $1 \times 1 \times 1.35\, mm^3$

Noise

In our study, we evaluate the noise for the phantoms "water + FDG" and "gelatin + FDG" across all its FOV. Data in figure 7 suggests that the noise value is similar for the two phantoms within all ROIs in study.

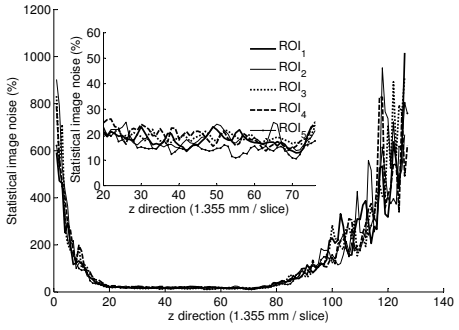

(a)

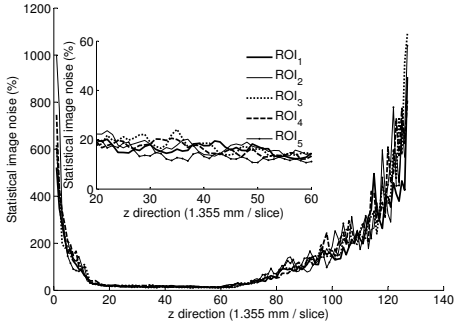

(b)

Fig. 7. Statistical image noise across all FOV in direction Z, for all study ROIs with 20 mm of diameter of phantom "water + FDG" (a) and "gelatin + FDG" (b) reconstructed with voxel size of $1 \times 1 \times 1.35\, mm^3$ and acquisition time of 15 min

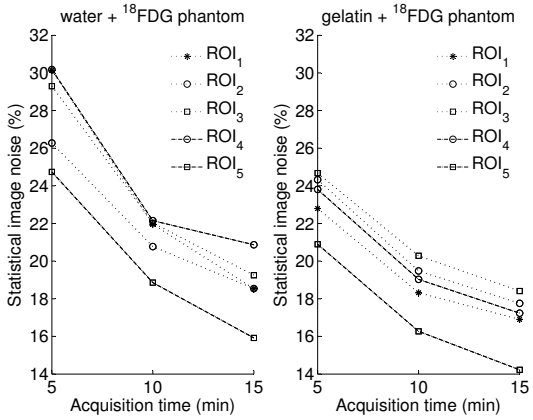

Fig. 8. COV (%) plotted versus acquisition time per detector orientation for phantom "water + FDG" (left) and "gelatin + FDG" (right) reconstructed with voxel size of $1 \times 1 \times 1.35\, mm^3$

Data obtained in studies of noise versus acquisition time, shown on figure 8, indicates that the values are correlated, as we expected. Less acquisition time contributes to noise increase because the statistics in each voxel is lower.

In order to deepen the understanding of the noise variation between voxels, we studied of the distribution of the number of counts per voxel in a central ROI with 3803 voxels ($\sim 15 \times 15 \times 20\, mm$). The distributions for the two phantoms ("water + FDG" and "gelatin + FDG") are plotted in the figure 9. As evidenced in this figure, the distributions are well described by a Gaussinan function. This means that most voxels (about 68%, assuming a normal distribution) are less than one standard deviation from the mean and so we can assume that there are not fluctuations or systematic non-Gaussian fluctuations between voxels.

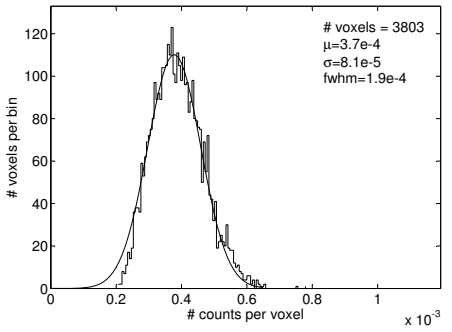

(a)

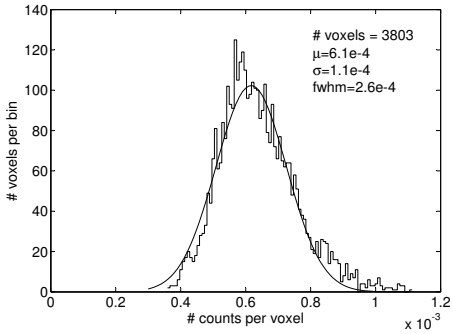

(b)

Fig. 9. Distribution of the number of counts per voxe of phantom "water + FDG" (a) and "gelatin + FDG" (b) reconstructed with voxel size of $1 \times 1 \times 1.35\, mm^3$ and acquisition time of 15 min

Lesion To Background Noise

Using the method described above, we studied several gelatin phantoms reconstructed with voxel size of $1 \times 1 \times 1.35\, mm^3$ and many acquisitions time.

The study of LTBN versus lesion diameters is displayed in figure 10. This analysis covers a phantom with lesions of 5, 10 and 15 mm of diameter and LTB = 10:1 and indicates that larger lesions entail an increase on LTBN. In face of these results, it is important to emphasize that lesion detectability is not only dependent on the detector performance but also on the biological characteristics of the tumor. For instance, it is known that a very small tumor usually contain lower amounts of activity due to its weak vascularity that jeopardize the radiotracer absorption, besides the natural variation in the tumor activity or LTB in each patient.

It was also performed the study of LTBN versus acquisition time. In that respect, we have analyzed gelatin phantoms with differents LTB and lesion sizes, with acquisition times of 2, 5, 8, 10, 13 and 15 minutes. The results in figure 11 show that LTBN values decrease slightly for lower acquisition times. For example, it can be seen that for an acquisition time of 15 minutes the LTBN is 12.78, while for 5 minutes is 11.43.

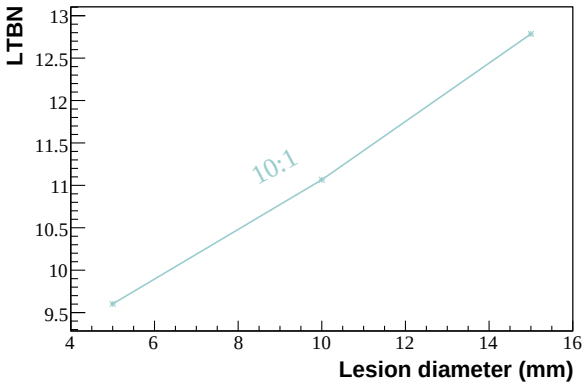

Fig. 10. LTBN plotted versus lesion diameter in a gelatin phantom of LTB = 10:1 reconstructed with voxel size of $1 \times 1 \times 1.35\, mm^3$ and acquisition time of 15 min

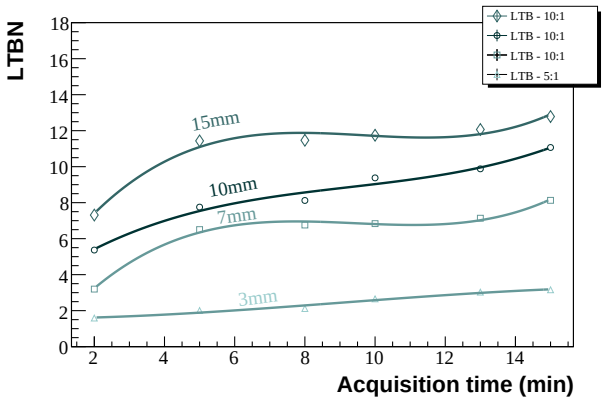

Fig. 11. LTBN plotted versus acquisition time in several gelatin phantom with diferents LTB and lesion size reconstructed with voxel size of $1 \times 1 \times 1.35\, mm^3$

These values are more proeminent in acquisition times of 2 minutes, where the LTBN drops to 7.31 in the same example.

The definition of LTBN = 3 as the threshold above which the background statistical fluctuations does not interfere with identification of lesions (because the probability of Gaussian statistical fluctuations above 3 standard deviations is about 0.1%), we conclude that the lesions studied obey this criterion for acquisition times greater than 2–3 minutes per detector orientation, except for lesions with 3 mm in diameter, which require acquisition times of 15 minutes. In the latter case we obtained LTBN = 2 with 5 min acquisition.

Contrast

The CRC(%) was studied for different LTBN and for different lesion sizes. In the first study, we found that a LTBN of 8–12 contribute to CRC in the range of 90%–100%, and lower LTBN give rise to CRC(%) above 85%, as shown in figure 12.

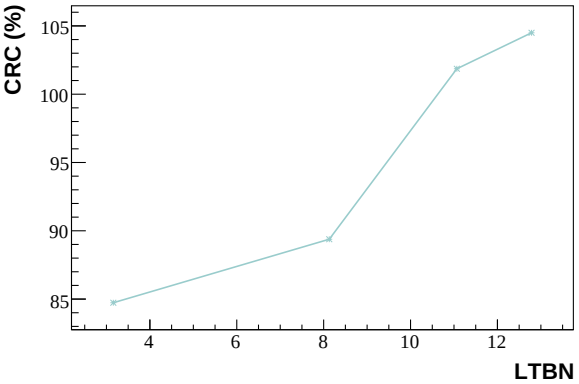

Fig. 12. CRC plotted versus LTBN in gelatin phantoms with diferents LTB and lesion size reconstructed with voxel size of $1 \times 1 \times 1.35\, mm^3$ and acquisition time of 15 min

Similar results were obtain with study of CRC versus lesions size. The figure 13 reports that diameter sizes above 10 mm contribute to values of CRC(%) close to 100%. This percentage decreases to about 70% when lesions have diameters size between 5 and 10mm, and smaller lesions have CRC (%) of 30%.

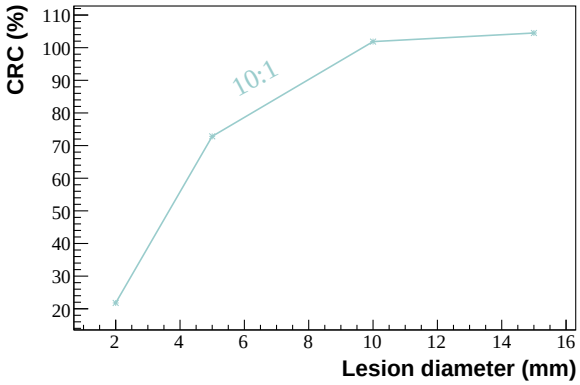

Fig. 13. CRC plotted lesions size in gelatin phantoms with diferents LTB and lesion size reconstructed with voxel size of $1 \times 1 \times 1.35\, mm^3$ and acquisition time of 15 min

Lesions size

We have analized the phantom "grid" reconstructed with voxel size of $1 \times 1 \times 1.35\, mm^3$ and of $2 \times 2 \times 1.35\, mm^3$, with and without a simple Gaussian filter. The figure 14 summarises this analysis.

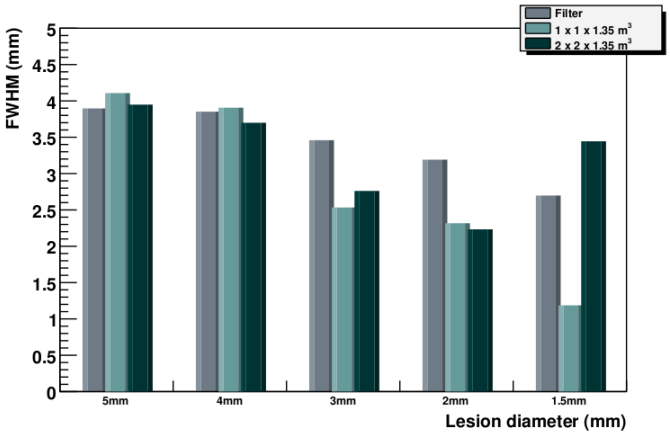

Fig. 14. Histogram of FWHM values of phantom "grid" reconstructed with voxel size of $1 \times 1 \times 1.35\, mm^3$ and $2 \times 2 \times 1.35\, mm^3$ and with and without simple Gaussian filter

It is apparent that in the majority of cases the FWHM values are similar among them and close to the lesion diameters; however, in images reconstructed with filter and voxel size of $2 \times 2 \times 1.35\, mm^3$, it can be observed a marked increase on FWHM in smaller lesions. These evidence indicate that the filter should not be applied because Gaussian smoothing reduces image noise but also reduces detail in image. On the other hand, as the small lesions are smaller than the voxel size

it is dificult to distinguish and detect them. We also found that the reconstruction of dimensions of the lesions is affected by the partial-volume effect. Variations of the real dimension of the smaller lesions are also expected due to the method of creating phantoms.

The analysis of phantom "grid + background" with LTB of 10:1, reconstructed with voxel size of $1 \times 1 \times 1.35\ mm^3$, without Gaussian filter and with acquisition time of 15 min, has shown that the FWHM values increase slightly compared with the same values where lesions is not surrounded by backgound (phantom "grid"), as it can be observed in table III.

Lesion size	FWHM (mm)	
	"grid"	"grid + background"
5 mm	4.1	4.8
4 mm	3.9	3.8
3 mm	2.5	3.1
2 mm	2.3	2.9
1.5 mm	1.2	2.1

TABLE III
FWHM VALUES FOR PHANTOM "GRID" AND PHANTOM "GRID + BACKGROUND" RECONSTRUCTED WITH VOXEL SIZE OF $1 \times 1 \times 1.35\ mm^3$ AND WITHOUT SIMPLE GAUSSIAN FILTER

In order to assess whether the process of placing lesions do degrade them or not, the phantom "cold" was studied and the values do not seem to be significantly different compared with of FWHM values of phantom "grid + background" (figure 15). Thus, we can say that the placement process is viable because it preserves the integrity of the lesions.

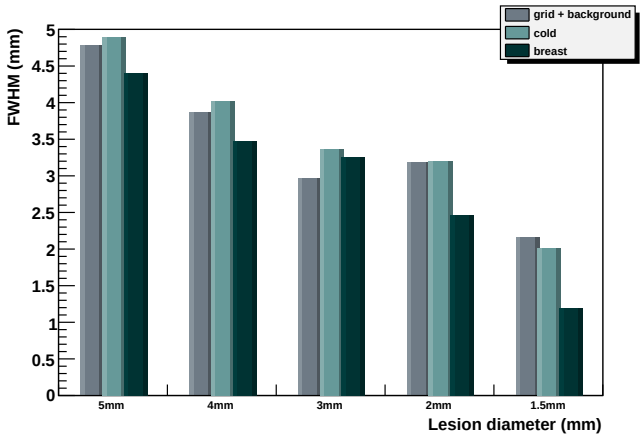

Fig. 15. Histogram of FWHM values of 4 phantoms reconstructed with voxel size of $1 \times 1 \times 1.35\,mm^3$ and $2 \times 2 \times 1.35\,mm^3$ and without simple Gaussian filter

To complete the study of lesions size, the analysis focused on a gelatin phantom with lesions of 5, 4, 3, 2 and 1.5 mm and LTB of 10:1 (phantom breast). As we expected, there seems to be a tendency of reduction of all FWHM values when lesions are surrounded by active background. This decrement is visible to all lesion sizes, being more noticeable in smaller lesions, as is evident in figure 15.

IV. CONCLUSIONS

We have presented a pre–clinical systematic evaluation of ClearPEM image quality. We have selected performance parameters that are relevant to the breast imaging application, like homogeneity, statistical noise, LTBN, contrast and lesion size. With the purpose of adapting to the caracteristics of breast tissue density gelatin phantoms with different lesion sizes and LTB ratios were created. All analyses were performed using ClearPEM device and reconstructed by STIR software, varying some parameters as voxel size and acquisition time.

Our results provide evidence that the ClearPEM images are globally homogeneous, with BV between 5–9%. In addition, the increased time of acquisition does not have a wide expression in BV, which allows shorter duration exams and, consequently, less discomfort for the patient. Satisfactory results were also obtained for the statistical noise showing that there are not statistical or systematic non-Gaussian fluctuations between voxels. We observed COV values of 20–24%. Thus, we can conclude that the statistical noise present in ClearPEM image does not interfere with the identification of lesions.

This study also indicates that the LTBN depends of the lesion size, being superior in larger lesions but it remaining practically the same with the decrease of acquisition time. Therefore, the ClearPEM allows for relatively short exams times, approximately 20 minutes in total.

Aditionally, our study reported CRC values over 90% for LTBN and lesion sizes in analaysis. The only results which may indicate some difficulties in detecting lesions are CRC values in the order of 30% for 3 mm lesions.

It is evident from the results of FWHM that we should use voxel size of $1 \times 1 \times 1.35\,mm^3$ and not use a simple Gaussian filter, otherwise we lose detectability in smaller lesions. It can also be concluded that the FWHM values are lower when lesions are surrounded by an active background, being this decrease more noticeable if the lesions are in direct contact with the background.

Our evaluation is across clinically acceptable range according to prior works documented in [12] [13] [14]. Improvements in the results are expected by the implementation of attenuation correction factors, so it would be interesting to reproduce the study in that conditions. Although this study has not analyzed the axillary area due to constraints on the head rotation of the detector, future works overcoming this limitation would be advantageous in order to compare results and extend the ClearPEM performance on breast cancer diagnosis.

In general, we can conclude that the creation process of gelatin phantoms is viable allowing for the simulation of breast cancer in a reliable and systematic way. As well the process of placement is viable because it preserves the integrity of the lesions. We can say that the detection of lesions is feasible down to 2 mm in diameter. The overall assessment of the detector opens a promising perspective for the use of ClearPEM technology in clinical practice, enabling greater detection power and patient comfort.

REFERENCES

[1] GfK HealthCare. Breast Cancer Survey. Online, 2011. http://www.siemens.com/press/pool/de/events/2011/healthcare/2011-03-ecr/studienergebnisse_breast_cancer.pdf.

[2] J.Xu E. Ward A. Jemal, R. Spiegel. Cancer statistics. *CA: A Cancer Journal for Clinicians*, pages 1542–4863, 2011.

[3] S. Manfred and A. Horst. Ultrasound imaging. *Phys. Med. Biol.*, 41:315–68, 2006.

[4] A. Karellas and S. Vedantham. Breast cancer imaging: A perspective for the next decade. *Medical physics*, 35:4878, 2008.

[5] C. Rose, J. Dose, and N. Avril. Positron emission tomography for the diagnosis of breast cancer. *Nuclear medicine communications*, 23(7):613, 2007.

[6] N. Avril, CA Rose, M. Schelling, J. Dose, W. Kuhn, S. Bense, W. Weber, S. Ziegler, H. Graeff, and M. Schwaiger. Breast imaging with positron emission tomography and fluorine-18 fluorodeoxyglucose: use and limitations. *Journal of Clinical Oncology*, 18(20):3495, 2000.

[7] J. Varela. A PET imaging system dedicated to mammography. *Radiation Physics and Chemistry*, 76(2):347–350, 2007.

[8] K. Schilling, P. Conti, L. Adler, and L. Tafra. The role of positron emission mammography in breast cancer imaging and management. *Applied Radiology*, 37(4):26, 2008.

[9] W.W. Moses. Positron emission mammography imaging. *Nuclear Instruments and Methods in Physics Research Section A: Accelerators, Spectrometers, Detectors and Associated Equipment*, 525(1-2):249–252, 2004.

[10] N. Avril, S. Bense, S.I. Ziegler, J. Dose, W. Weber, C. Laubenbacher, R. Omer, and F. Schwaiger J. Anicke. Breast imaging with flourine-18-FDG PET: quantitative image analysis. *The Journal of nuclear medicine*, 38(8):1186–1191, 1997.

[11] C. Ortigo. *ClearPEM Procedures Manual – Verso4.1*. 2012.

[12] S. Tong, AM Alessio, and PE Kinahan. Noise and signal properties in PSF-based fully 3D PET image reconstruction: an experimental evaluation. *Physics in medicine and biology*, 55:1453, 2010.

[13] N.A. Shkumat, A. Springer, C.M. Walker, E.M. Rohren, W.T. Yang, B.E. Adrada, E. Arribas, S. Carkaci, H.H. Chuang, L. Santiago, et al. Investigating the limit of detectability of a positron emission mammography device: A phantom study. *Medical Physics*, 38:5176, 2011.

[14] A. Springer and O.R. Mawlawi. Evaluation of the quantitative accuracy of a commercially available positron emission mammography scanner. *Medical Physics*, 38:2132–2139, 2011.